PAPER

Check for updates

Departmental characterization of structural and mechanical properties of crossed lamellae of a gastropod *Murex pecten*†

Naotake Nishio,[a] So Sugiyama,[a] Taro Yoshimura,[ab] Ryunosuke Terasaki,[a] Mihiro Takasaki, [iD][a] Yuya Oaki, [iD][a] Takenori Sasaki[b] and Hiroaki Imai [iD] *[a]

We characterized departmental variations of the hierarchical lamellar structures of whorls, a siphonal canal, and spines of shells of a gastropod *Murex pecten* (Venus comb) and compared their mechanical properties. The crossed lamellae are basically composed of bundled aragonite nanorods ~20 nm wide that are elongated along the (110) plane. The main body, including whorls and a siphonal canal, consists of four- and three-layer crossed lamellae, and thin spines comprise double- and single-layered structures including strained and distorted lamellae. The macroscopic bending strength and nanoscopic hardness of the spines were found to be greater than those of the main body of the shell. The specific strained and distorted lamellar structures are deduced to contribute to the enhanced mechanical properties of the long and thin parts.

Introduction

Biological minerals, such as shells and bones, are composite materials made of inorganic and organic components produced by living organisms.[1,2] The sophisticated architectures of various shells and bones have several functions for the protection and framing of their bodies. The hierarchical minerals are produced throughout the biomineralization processes under ambient aqueous conditions where the polymorph, size, and shape of the crystal building blocks of biominerals are controlled by biogenic organic molecules.[3–9] The clarification and mimicking of biogenic architectures are important to develop environmentally friendly technologies for the production of novel functional materials consisting of calcium-based minerals.

The tough and hard nature of gastropod shells is ascribed to crossed lamellar structures in which aragonitic calcium carbonate and a small fraction (~1–5%) of organic components are organized in sheets.[10] The fibrous aragonite crystallites in one sheet are oriented at relatively high angles to adjacent sheets. In general, the complicated hierarchical architectures are associated with toughening of crystals.[11–15] The hardness variations in the different layers of crossed lamellar structures were found to be related to the crystallographic orientation of the aragonite crystal.[16–18] The fracture mechanisms of the crossed lamellar layers were discussed in light of the alignment and orientation of the interfaces. However, departmental variations in the construction and strains of the crossed lamellar structures at macro- and microscales have not been sufficiently studied for clarification of the mechanical properties of shells. Particularly, biomineral spines, represented by gastropods, are a frequently acquired trait in diverse lineages of animals with carbonate skeletons. Therefore, these tough and hard properties, instead of a long and thin morphology, should have advantages for a biomineral material and can be studied to help in the useful fabrication of light-weight high-strength materials.

In this study, we investigated the hierarchical architectures and their mechanical properties of aragonitic shells of a marine gastropod, *Murex pecten*, commonly known as the Venus comb. The departmental variations in crossed lamellar structures in whorls, a siphonal canal, and spines were clarified through the characterization of bundled aragonite nanorods using scanning electron microscopy (SEM) and Raman scattering spectroscopy. Moreover, we compared the bending strength, hardness, and modulus of various parts of the shell. Here the specific mechanical properties of long,

[a] Department of Applied Chemistry, Faculty of Science and Technology, Keio University, 3-14-1 Hiyoshi, Kohoku-ku, Yokohama 223-8522, Japan. E-mail: hiroaki@applc.keio.ac.jp
[b] The University Museum, The University of Tokyo, 7-3-1 Hongo, Bunkyo-ku, Tokyo 113-0033, Japan

† Electronic supplementary information (ESI) available: Schematic and SEM images of a cross-section of a siphonal canal (Fig. S1); XRD patterns for powdery and fractured samples of a shell of *Murex pecten* shell (Fig. S2); SEM and IPF mapping images and the pole figure of the end of the sheet as a unit of the 1st lamella (Fig. S3); Raman scattering spectra of the crossed lamellar structures (Fig. S4); the contents of organic molecules in the crossed lamellar structures estimated form thermal gravimetry curves of the samples (Fig. S5); schematic illustration and SEM image of the crossed lamellar structure for indicating the indentation directions (Fig. S6); photos and schematic illustrations of samples for the bending test (Fig. S7); force curves of bending test samples (Fig. S8). See DOI: https://doi.org/10.1039/d3ce00177f

thin spines were discussed, along with influence of distorted morphology, lattice strain, and organic contents. These results would provide a hint for the design of biomimetic devices consisting of common carbonate crystals.

Results & discussion

Macroscopic architectures of the shell of *Murex pecten*

Fig. 1 illustrates macroscopic layer structures of whorls, a siphonal canal, and spines with a photo of the whole shell of *Murex pecten*. Here, we consider variations in the layered
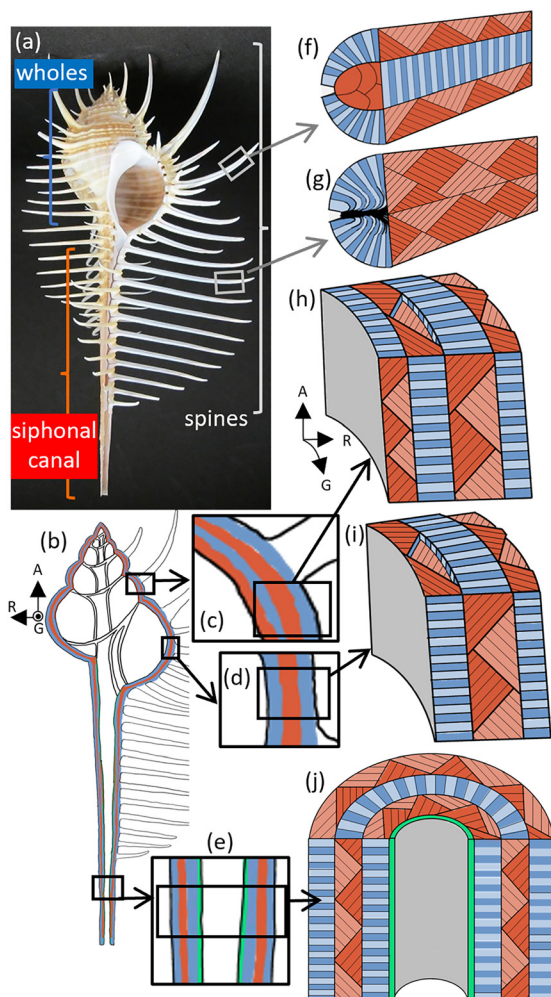
constructions; a detailed characterization of the parts is given in the following sections.

We observed four and three layers consisting of crossed lamellae in the main shell body (Fig. 1a–e and h–j). The multilayers are constructed by the stacking of differently oriented lamellae (blue and orange layers). The upper and lower parts of the whorls are composed of four and three distinct layers, respectively (Fig. 1b–d, h and i). The fibrous units in one layer are normally oriented to adjacent layers. The innermost layer of the upper whorls is inferred to be formed through additional shell growth. The siphonal canal is a tube consisting of three bending layers of the lamellae (Fig. 1b, e and j) with a prismatic layer as the innermost coat (Fig. S1 in the ESI†). Spines that are projected from the whorls consist of a double-layered lamella (Fig. 1f), whereas spines on the siphonal canal are composed of a single-layered lamella (Fig. 1g). Since the spines have a rounded outer form, the lamellae are highly distorted in the cladding areas.

Basal structures of lamellae

Fig. 2 shows SEM images and schematic illustrations of the basal lamellar structure of *Murex pecten*. The macroscopic layers shown in Fig. 1 are composed of numerous parallel
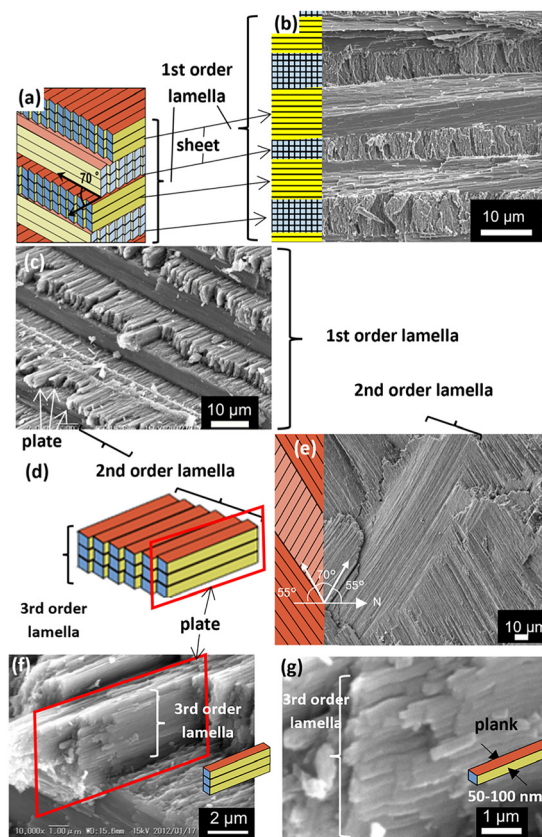

Fig. 1 Schematic illustrations of macroscopic layers of whorls, a siphonal canal, and spines with a photo of *Murex pecten*. (a) A photo and (b) an illustration of a cross section of the whole body. Detailed illustrations of (c and h) the four-layer lamella of the upper part and (d and i) the three-layer lamella of the lower parts of whorls, (e and j) the three-layer lamella with a prismatic layer of a siphonal canal, (f) the double-layer lamella of a spine on the whorls, and (g) the single-layer lamella of a spine on the siphonal canal. Blue and red parts show the cross sections exposing the top and side faces of the basal sheets, respectively (see Fig. 2). The contrast in density indicates the difference in the directions. The green part in the siphonal canal shows a prismatic layer (Fig. S1 in the ESI†). A: The axial direction; G: the shell growth direction; R: the radial direction.

Fig. 2 SEM and schematic illustrations of the basal lamellar structure of *Murex pecten*. (a and b) The 1st-, (c–e) 2nd-, and (f and g) 3rd-order lamellae.

sheets with a thickness of 4–15 μm (1st-order lamella: blue, pale blue, and yellow regions in Fig. 2a–c), which consist of unidirectional plate arrays (orange and pale orange regions in Fig. 2d and e). The sheets consist of rectangular plates with a thickness of 1–2 μm and a length of several hundred micrometers (2nd-order lamella). The difference in plate direction between the upper and lower sheets is *ca.* 70° (Fig. 2a and e). As shown in Fig. 2f and g, the plates are comprised of bundled rectangular planks with a width of ∼100 nm (3rd-order lamellae). The architecture at four orders of hierarchy (macroscopic layers, sheets, plates, and nanoscopic planks), which is observed in the all parts of the shell, is basically the same as those reported for other shells.[19,20]

All the parts of the shell were assigned to aragonitic calcium carbonate based on X-ray diffraction (XRD) patterns (Fig. S2 in the ESI†). Since an intense 110 signal was observed in the diffraction pattern from a section exposing bundled nanorods of the sheets (the orange face) in the 1st-order lamellae, the plane is deduced to be (110).

Fig. 3 shows the crystallographic information of the end of a sheet as a unit of the 1st-order lamella. We observed parallel planks that comprise the 3rd-order lamella in the SEM image (Fig. 3c). The pole figure (Fig. 3b) and the inverse pole figure (IPF) map for A (the axial direction) (Fig. 3d) suggest that the *c* direction deviates from the long axis of the planks whereas the strict angle is not clarified. The blue-green structure on the IPF map for G (the shell growth direction) indicates that the orange face is (110) (Fig. 3e). These results are consistent with the estimation based on the XRD patterns (Fig. S2 in the ESI†) and the crystallographic direction of the nanoscopic planks of other gastropods reported in a previous work.[21]
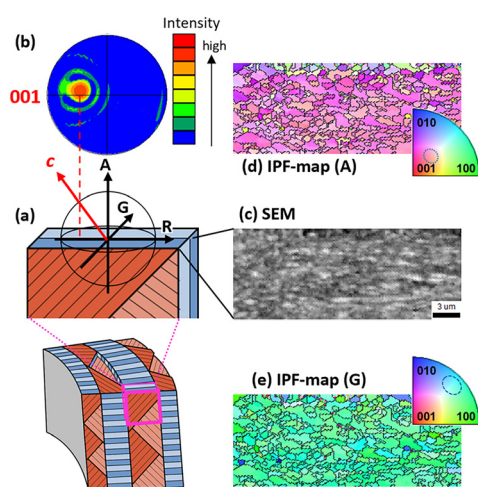
Details of the lamellae of the whorls, siphonal canal, and spines

The whorls and the siphonal canal are basically composed of inner, middle, and outer layers (Fig. 4). In the inner and outer layers, the sheets of the 1st-order lamellae are aligned normal to A (the axial direction) and parallel to G (the shell growth direction) and R (the radial direction) (Fig. 4a, b, d, f, g and j). The lamellae in the middle layer are aligned normal to G and parallel to A and R. The directions of the plates in the 2nd-order lamellae are aligned ±55° from R (Fig. 2e). The innermost layer of the upper whorls is inferred to be formed through additional shell growth. The lamellae in innermost layer are also aligned normal to G and parallel to A and R. The macroscopic curvature of the crossed lamellae in the siphonal canal is greater than that in the whorls (Fig. 4a, b, f and g), while the basal three-layered structures are the same in both parts.

The spines on the whorls consist of a double-layered lamella that is separated into a core and a clad (Fig. 5a–e). The sheets that comprise the 1st-order lamella are radially aligned and parallel to the elongated direction of the spine in the clad and they are aligned normal to the core. Since the spines have a rounded outer form, the lamellae are highly distorted. As shown in the cross-sectional SEM image of the spines (Fig. 5g–j), we found curved bundles in the 2nd-order lamellae in the inner layer.

The spines on the siphonal canal are composed of single-layered lamellae (Fig. 5k–p) that have the same structure as the clad of the spines on the whorls. The sheets that comprise the 1st-order lamella are radially aligned and parallel to the elongated direction.
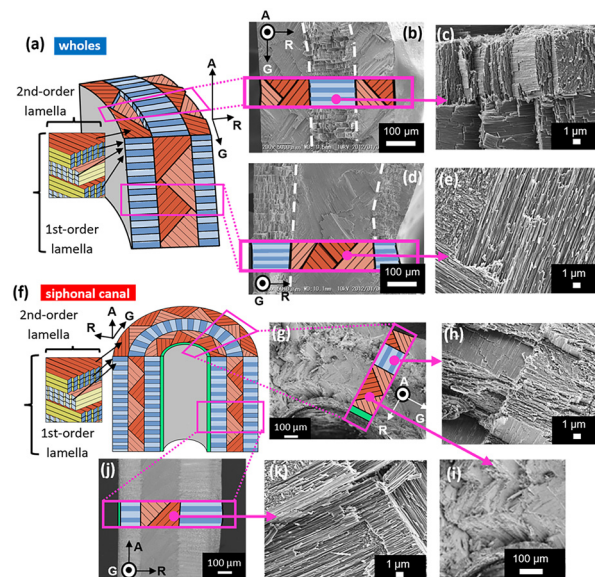

Fig. 3 SEM and IPF mapping images and the pole figure of the end of the sheet as a unit of the 1st lamella. (a) Schematic illustrations of the sample; (b) the pole figure from the *A* direction; (c) an SEM image observed from A; (d) an IPF mapping image for A; (e) an IPF mapping image for G. The IPF mapping image for R is shown in Fig. S3 in the ESI.†

Fig. 4 Schematic illustrations and SEM images of the detailed structures of the 1st- and 2nd-order lamellae of the whorls and siphonal canal. (a) Schematic illustrations and (b–e) SEM images of the whorls; (f) schematic illustrations and (g–k) SEM images of the siphonal canal.
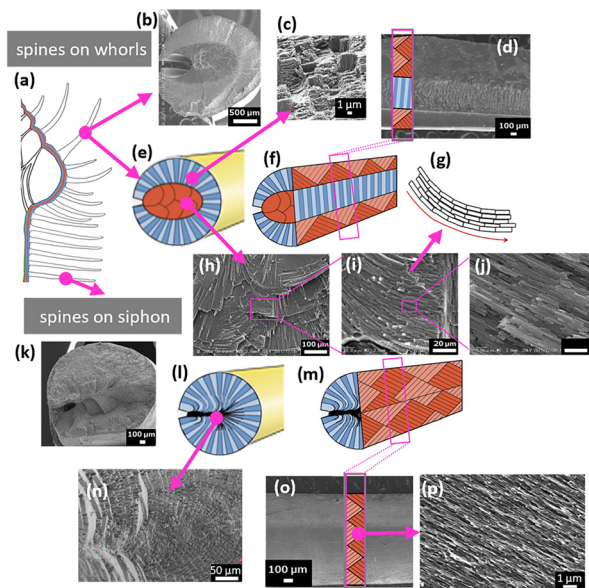
Fig. 5 SEM and schematic images of cross sections of spines. (a) Schematic illustration of the spines on the whorls and siphonal canal; (b–j) SEM images and illustrations of the spines on the whorls; (b, c and e) the transverse plane and (d and f) the longitudinal plane; (c) an enlarged image of the clad and (g–j) enlarged images of the core in (b). (k–p) SEM images and illustrations of the spines on the siphonal canal; (k, l and n) the transverse plane and (m, o and p) the longitudinal plane.

Nanoscopic characterization of the whorls, siphonal canal, and spines

We examined the crystallinity of the aragonite nanoplanks by using Raman scattering spectroscopy. Several specimens of the crossed lamellar structures were etched with ethylene diamine tetraacetate (EDTA) to remove damaged surface layers. We obtained specific signals due to the lattice vibration that is assigned to aragonite (Fig. 6a). The variation of the signals to a lower wavenumber indicates the presence of a tensile strain of the lattice[22] for the lamellar structures (Raman spectra indicating detailed variation were shown in Fig. S4 in the ESI†). Particularly, the tensile strain of the
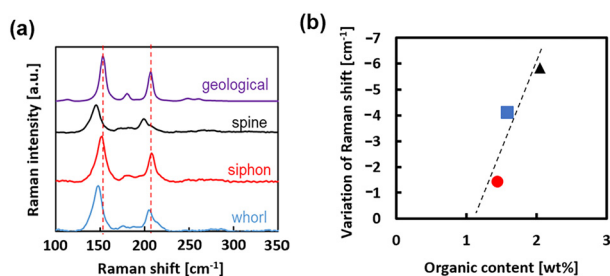
spines is greater than that of the other parts. The variation of the Raman signal increased steeply with the increasing organic content (Fig. 6b). The presence of the basal organic content (∼1.2 wt%) is not related to the Raman shift as the x-intercept. This suggests that small amounts of organic compounds are located outside the crystal lattices, such as in the gaps between aragonite planks. The crossed lamellae were reported to contain amino acids, such as aspartic acid and glycine.[23,24]

Mechanical properties of the whorls, siphonal canal, and spines

We evaluated the hardness (H) and Young's modulus (E) for the crossed lamellar structures of whorls, a siphonal canal, and spines using a nanoindentation technique (Fig. 7). The evaluation was performed in two directions: parallel (∥) and normal (⊥) to the sheet of the 1st-order lamella (Fig. S6 in the ESI†). Basically, the H and E values for the direction parallel (∥) to the long axis of aragonite planks were higher than those for the direction perpendicular to the axis (⊥). These results are consistent with those of previous works.[19] The mechanical property depending on the crystallographic direction is known for mineral aragonite. The H values with the direction parallel and normal to the sheets are close to those of the mineral with the direction parallel (∼6 GPa) and normal (∼3 GPa) to the c-axis, respectively.

The H value (∥) with the parallel direction increased as the tensile strain increases (Fig. 7a). Thus, the aragonite crystal is hardened by increasing the organic content in the lattice. Finally, the spines containing greater amounts of organic components are inferred to be harder than the other parts. However, the H value (⊥) did not change with the organic content or lattice strain. The width of the planks is suggested to be insufficient as an interaction length for the variation in the macroscopic mechanical property.

The E values (∥: ∼80 GPa, ⊥: ∼30 GPa) are much lower than those of the mineral for both parallel and perpendicular directions to the c-axis (∥: ∼100 GPa; ⊥: ∼80 GPa). The variation in E values with the strain was not remarkable (Fig. 7b). Thus, the decrease in the E value is ascribed to the

Fig. 6 (a) Raman scattering spectra for the spine, siphonal canal, and whorl of *Murex pecten* after EDTA etching. Raman spectra from 100 to 1200 cm⁻¹ and from 100 to 250 cm⁻¹ are shown in Fig. S4 in the ESI.† (b) The shift in the Raman signal as a function of the organic content of the shell. The organic content was evaluated based on the thermal gravimetry curves (Fig. S5 in the ESI†).
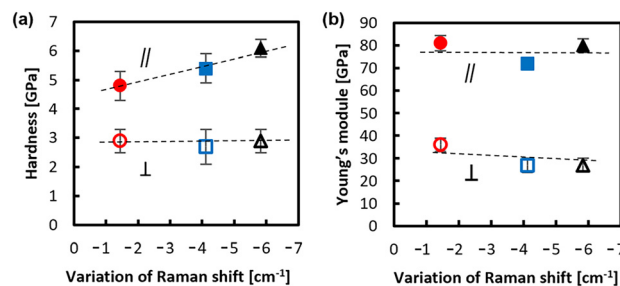

Fig. 7 (a) The hardness (H) and (b) Young' modulus (E) as a function of the Raman shift variation of the crossed lamellar structures of a *Murex pecten* shell. Circles: whorls; squares: the siphonal canal; triangles: spines. (∥) Parallel and (⊥) normal to the sheet of the 1st-order lamella.
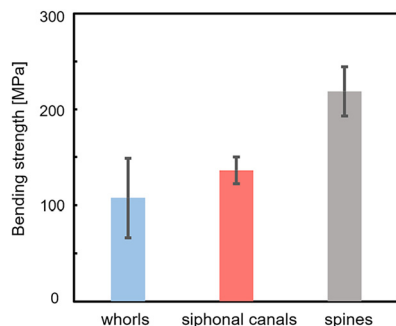
Fig. 8 The bending strength of whorls, siphonal canals, and spines of a *Murex pecten*. The configuration of the samples for the bending test and the force curves are shown in Fig. S7 and S8,† respectively, in the ESI.†

presence of the organic components outside the crystalline rods in the lamellar structures. The combination of the low-modulus portions drastically decreases the total modulus of the composites. However, further investigation including detailed characterization of the minor components is required to clarify the influence of the organic matter on the mechanical properties.

The mechanical property of the lamellae depends on the direction. Thus, the three- and four-layer lamellae of the whorls and siphonal canal are important for reinforcement of the shell in all directions. Moreover, the propagation of cracks is suppressed by the boundaries between the lamellar layers. We evaluated the macroscopic strength of three parts of the shell using a three-point bending test (Fig. S7 in the ESI†). Fig. 8 shows the bending strength of the whorls, siphonal canal, and spines. The fracture strength of spines having a single-layer lamella is clearly greater than that of the whorls and siphonal canal having three-layer lamellae. The particular property of the spines is ascribed to the bending morphology of the lamellae (Fig. 5) with higher lattice strains (Fig. 6a). The siphonal canal is stronger than the whorls, although the hardness and lattice strain of the canal part are lower than those of the main body. This suggests that the curved lamellar structure is essential for the strengthening of the crossed lamellae. The propagation of cracks is suppressed by the distorted boundaries between the lamellar layers.

Conclusions

We studied the hierarchical architectures and mechanical properties of aragonitic shells of a gastropod, *Murex pecten*. We observed a significant influence of lamella orientation and lattice strain on the mechanical properties. The lattice strain and the curved morphology of aragonite crystals increase the hardness of the crossed lamellar structures and the bending strength of the whole body. Particularly, the higher hardness and bending strength of the spines newly explain the material mechanical factors that allow them to withstand external loads despite their obvious slender structure.

Experimental

Murex pecten (Venus comb) shells were obtained from a commercial shell vendor. Specimens were sectioned using a rotary tool with a diamond-embedded cutoff wheel. Several samples were crushed and treated with a sodium hypochlorite aqueous solution (5.0 wt% $NaClO_{aq}$) to remove organic matter. We used a field-emission SEM (JEOL JSM-7600F) operated at 5.0 kV to observe the meso- and nanostructures of the surface and cross section of the shells. The surfaces and cross-sections of crushed samples were etched with a 0.1 wt% ethylene diamine tetraacetate solution to remove damaged topmost layers and then coated with osmium for SEM observation. We evaluated the crystal structure and composition of the shell using X-ray diffractometry (XRD, Bruker D8 Advance), Raman scattering spectroscopy (Renishaw inVia Raman microscope), and thermal gravimetry (Shimadzu DTG-60). The spectral resolution of the Raman scattering spectrometer is 1 cm^{-1}. Thus, the variation of the Raman signals that was observed in the present study is outside the resolution. The Raman signals were not influenced by the sample surface features because the signal positions were not shifted by the change in the part of the samples. Basically, we used large spines on whorls for Raman scattering spectroscopy. However, the crystallinity and nanostructures of the spines on whorls and a siphon canal are almost the same. Microstructure and texture characterization of the crossed lamellae was based on electron backscatter diffraction (EBSD) measurements. Shell samples were embedded in epoxy resin and subjected to several sequential mechanical grinding and polishing steps, with the final step consisting of an etch-polishing with colloidal silica. EBSD measurements were carried out, after coating with osmium, on a JEOL JSM-70001F field-emission SEM equipped with an Oxford EBSD detector. Information obtained from EBSD measurements is presented as color-coded crystal-orientation maps with corresponding pole figures.

Nanoindentation was performed using a Hysitron TI-950 nanoindenter equipped with diamond-cube corner probes. Sections were embedded in epoxy resin and polished with diamond suspensions for nanoindentation. Specimens for the three-point bending test were excised from the three parts of a shell using a low-speed diamond saw and then carefully ground. Three-point bending tests were conducted at room temperature with a constant displacement rate of 0.001 mm s^{-1} using an Instron 5944 testing machine. The sample dimension was 10.0 mm × 2.0 mm × 1.5 mm with a gauge length of 8 mm. Ten samples each from at least three individuals were prepared for each part to ensure good reliability.

Conflicts of interest

There are no conflicts to declare.

Acknowledgements

Notes and references

1 Z. Deng, Z. Jia and L. Li, *Adv. Sci.*, 2022, **9**, 2103524.

2 U. G. K. Wegst, H. Bai, E. Saiz, A. P. Tomsia and R. O. Ritchie, *Nat. Mater.*, 2015, **14**, 23–36.

3 N. Watabe, *J. Cryst. Growth*, 1974, **24/25**, 116–122.

4 M. Gills, A. Meibom, I. Domart-Coulon, O. Grauby, J. Strolarski and A. Baronnet, *J. Morphol.*, 2014, **275**, 1349–1365.

5 C. Moureaux, A. Perez-Huerta, P. Compere, W. Zhu, T. Leloup, M. Cusack and P. Dubois, *J. Struct. Biol.*, 2010, **170**, 41–49.

6 A. Lin and M. A. Meyers, *Mater. Sci. Eng., C*, 2005, **390**, 27–41.

7 D. E. Jacob, A. L. Soldati, R. Wirth, J. Huth, U. Wehrmeister and W. Hofmeister, *Geochim. Cosmochim. Acta*, 2008, **72**, 5401–5415.

8 F. Nudelman, H. H. Chen, H. A. Goldberg, S. Weiner and L. Addadi, *Faraday Discuss.*, 2007, **136**, 9–25.

9 A. B. Rodriguez-Navarro, A. Checa, M. G. Willinger, R. Bolmaro and J. Bonarski, *Acta Mater.*, 2012, **8**, 830–835.

10 L. Addadi, D. Joester, F. Nudelman and S. Weiner, *Chem. – Eur. J.*, 2006, **12**, 980–987.

11 L. Li and C. Ortiz, *Nat. Mater.*, 2014, **13**, 501–507.

12 S. Kamat, X. Su, R. Ballarini and A. H. Heuer, *Nature*, 2000, **405**, 1036–1040.

13 L. T. KuhnSpearing, H. Kessler, E. Chateau, R. Ballarini and A. H. Heuer, *J. Mater. Sci.*, 1996, **31**, 6583–6594.

14 R. Menig, M. H. Meyers, M. A. Meyers and K. S. Vecchio, *Mater. Sci. Eng., A*, 2001, **297**, 203–211.

15 X. W. Li, H. M. Ji, W. Yang, G. P. Zhang and D. L. Chen, *J. Mech. Behav. Biomed. Mater.*, 2017, **74**, 54–71.

16 C. L. Salinas, E. E. Obaldia, C. Jeong, J. Hernandez, P. Zavattieri and D. Kisailus, *J. Mech. Behav. Biomed. Mater.*, 2017, **76**, 58–68.

17 W. Yang, G. P. Zhang, X. F. Zhu, X. W. Li and M. A. Meyers, *J. Mech. Behav. Biomed. Mater.*, 2011, **4**, 1514–1530.

18 L. Romana, P. Thomas, P. Bilas, J. L. Mansot, M. Merrifiels, Y. Bercion and D. A. Aranda, *Mater. Charact.*, 2013, **76**, 55–68.

19 D. F. Hon, G. S. Zhou and M. Zheng, *Biomaterials*, 2004, **25**, 751–756.

20 H. M. Ji, Y. Jiang, W. Yang, G. P. Zhang and X. W. Li, *J. Am. Ceram. Soc.*, 2015, **98**, 3319–3325.

21 T. Kogure, M. Suzuki, H. Kim, H. Mukai, A. G. Checa, T. Sasaki and H. Nagasawa, *J. Cryst. Growth*, 2014, **397**, 39–46.

22 P. Gillet, C. Biellmann, B. Raynard and P. McMillan, *Phys. Chem. Miner.*, 1993, **20**, 1–18.

23 B. Pokroy, E. Zolotoyabko and N. Adir, *Biomacromolecules*, 2006, **7**, 550–556.

24 I. Kobayashi and T. Samata, *Mater. Sci. Eng., C*, 2006, **26**, 692–698.